Comptes Rendus
Mécanique
0000, 1, nº 0, p. 000-000
DOI unassigned yet

StandardLayout=true

Numerical experiments on manifold learning, manifolds dimension and latent variables

Ruben Ibanez [a], Pierre Gilormini [b], Elias Cueto [c] and Francisco Chinesta [d]

[a] PIMM lab, Arts et Metiers Institute of Technology, 151 Boulevard de Hôpital, 75013 Paris, France

[b] PIMM lab, Arts et Metiers Institute of Technology, 151 Boulevard de Hôpital, 75013 Paris, France

[c] Aragon Institute of Engineering Research, Universidad de Zaragoza, Maria de Luna s/n, 50018 Zaragoza, Spain

[d] PIMM lab, Arts et Metiers Institute of Technology, 151 Boulevard de Hôpital, 75013 Paris, France.

E-mails: Ruben.IBANEZ-PINILLO@ensam.eu (R. Ibanez), Pierre.GILORMINI@ensam.eu (P. Gilormini), ecueto@unizar.es (E. Cueto), francisco.chinesta@ensam.eu (F. Chinesta).

Abstract. The present work aims at analyzing issues related to the data manifold dimensionality, with a double interest: (i) first, when too many measurable variables are considered, manifold learning is expected to extract the useless ones; (ii) second, and more important, the same technique, manifold learning could be employed for informing on the necessity of employing latent extra-variables able to recover single-valued outputs.

Keywords. Manifold Learning, State variables, Dimensionality reduction, *k*-PCA.
Funding. First author is supported by CREATE-ID ESI-ENSAM research chair.
The third author is supported by the ESI Group Chair at the University of Zaragoza.
Fourth author is supported by CREATE-ID ESI-ENSAM research chair.

This article is a draft (not yet accepted!)

1. Introduction

Recently, data-driven description of materials is gaining popularity. Many complex material behaviors resisting traditional modeling procedures, or being too complex from a microstructural viewpoint, are being approached by using data-based descriptions. Different approaches are being considered. Among them, the ones based exclusively on the measured data, others extracting the manifolds related to the data, others looking for enforcing thermodynamics consistency, ...

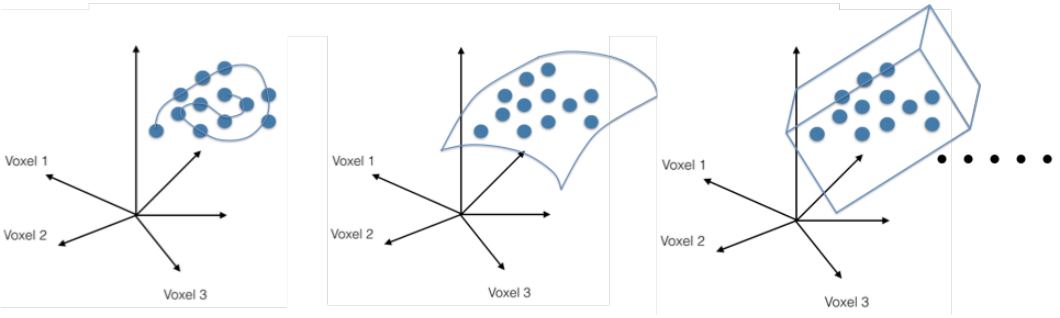

Figure 1. Multi-dimensional data on a one- (left), two- (center), three-dimensional (right) manifold embedded in $\mathbb{R}^D$.

[6, 2, 9, 3, 4, 7]. This work focusses on techniques based on the use of manifolds and their associated manifold learning procedures for extracting them from the available data.

In general data involve many dimensions. Imagine for a while a sequence of three-dimensional fields defined in a domain $\Omega \subset \mathbb{R}^3$ partitioned into D voxels. Each of these fields contains many data, one datum at each voxel. Each field can be represented as a point in a vector space of dimension D (the number of voxels), where we could imagine each of the D coordinate axes as reporting the value that the field of interest takes in the associated voxel. Thus, each field becomes a point in that high-dimensional space of dimension D, $\mathbb{R}^D$. If important correlations exist among the different fields, these points are expected to be distributed on a low-dimensional subspace embedded into the D-dimensional space. Techniques aiming at extracting these reduced subspaces, the so-called slow-manifolds, sketched in Fig. 1, are key tools for manipulating data and extracting their hidden information.

Thus, data define in general slow-manifolds embedded in very large vector spaces due to the significant hidden correlations among them. The number of uncorrelated explicative dimensions becomes in general much smaller than the “a priori" assumed dimension of the space for accommodating the data. The extraction of these slow-manifolds can be successfully accomplished by using linear and nonlinear dimensionality reduction techniques, like Principal Component Analysis (PCA) in the linear case, and its nonlinear counterparts (e.g. ℓPCA, k-PCA, LLE, tSNE, ...) [8, 10, 11, 5, 12].

These techniques can be applied to several physical systems and as soon as the slow-manifold is determined, the solution at any point on it can be very accurately computed from a simple interpolation of neighbor data on the manifold [1], enabling almost real-time predictions and the associated real-time decision-making.

However, extracting knowledge from data associated to an existing but hidden model requires

- Identifying the manifold intrinsic dimension,
- Discovering hidden parameters,
- Discarding useless parameters,
- Discovering the models originating the data.

These questions will be addressed, illustrated and discussed in the present work, at present purely methodologically, aiming at illustrating the key concepts that could open numerous future possibilities, in the field of mechanics of materials, processes, structures and systems.

2. Manifold Learning: From Principal Component Analysis to its kernel-based counterpart

2.1. *Principal Component Analysis, PCA*

Let us consider a vector $\mathbf{y} \in \mathbb{R}^D$ containing experimental results or synthetic data coming from numerical simulation. These results are often referred to as *snapshots*. If they are obtained by numerical simulation, they consist of nodal values of the essential variable. Therefore, these variables will be somehow correlated and, notably, there will be a linear transformation $\mathbf{W}$ defining the vector $\boldsymbol{\xi} \in \mathbb{R}^d$, with $d < D$, which contains the still unknown *latent variables*, such that

$$\mathbf{y} = \mathbf{W}\boldsymbol{\xi}. \tag{1}$$

The $D \times d$ transformation matrix $\mathbf{W}$, that satisfies the orthogonality condition $\mathbf{W}^T\mathbf{W} = \mathbf{I}_d$, is the main ingredient of the Principal Component Analysis (PCA) [8].

Assume that there exist $\mathtt{M}$ different snapshots $\mathbf{y}_1, \ldots, \mathbf{y}_\mathtt{M}$, which we store in the columns of a $D \times \mathtt{M}$ matrix $\mathbf{Y}$. The associated $d \times \mathtt{M}$ reduced matrix $\boldsymbol{\Xi}$ contains the associated vectors $\boldsymbol{\xi}_i$, $i = 1, \ldots, \mathtt{M}$.

PCA works usually with centered variables. In other words,

$$\begin{cases} \sum_{i=1}^{\mathtt{M}} \mathbf{y}_i = \mathbf{0} \\ \sum_{i=1}^{\mathtt{M}} \boldsymbol{\xi}_i = \mathbf{0} \end{cases}, \tag{2}$$

implying the necessity of centering data before applying the PCA.

PCA proceeds by guaranteeing maximal preserved variance and minimal correlation in the latent variable set $\boldsymbol{\xi}$. The latent variables in $\boldsymbol{\xi}$ will therefore be uncorrelated, and consequently the covariance matrix of $\boldsymbol{\xi}$,

$$\mathbf{C}_{\xi\xi} = \mathrm{E}\{\boldsymbol{\Xi}\boldsymbol{\Xi}^T\}, \tag{3}$$

should be diagonal.

To extract the d uncorrelated latent variables we proceed from

$$\mathbf{C}_{yy} = \mathrm{E}\{\mathbf{Y}\mathbf{Y}^T\} = \mathrm{E}\{\mathbf{W}\boldsymbol{\Xi}\boldsymbol{\Xi}^T\mathbf{W}^T\} = \mathbf{W}\mathrm{E}\{\boldsymbol{\Xi}\boldsymbol{\Xi}^T\}\mathbf{W}^T = \mathbf{W}\mathbf{C}_{\xi\xi}\mathbf{W}^T. \tag{4}$$

Pre- and post-multiplying by $\mathbf{W}^T$ and $\mathbf{W}$, respectively, and making use of the fact that $\mathbf{W}^T\mathbf{W} = \mathbf{I}$, gives us

$$\mathbf{C}_{\xi\xi} = \mathbf{W}^T\mathbf{C}_{yy}\mathbf{W}. \tag{5}$$

The covariance matrix $\mathbf{C}_{yy}$ can then be factorized by applying the singular value decomposition,

$$\mathbf{C}_{yy} = \mathbf{V}\boldsymbol{\Lambda}\mathbf{V}^T, \tag{6}$$

with $\mathbf{V}$ containing the orthonormal eigenvectors and $\boldsymbol{\Lambda}$ the diagonal matrix containing the eigenvalues, sorted in descending order.

Substituting Eq. (6) into Eq. (5), we arrive at

$$\mathbf{C}_{\xi\xi} = \mathbf{W}^T\mathbf{V}\boldsymbol{\Lambda}\mathbf{V}^T\mathbf{W}. \tag{7}$$

This equality holds when the d columns of $\mathbf{W}$ are taken colinear with d columns of $\mathbf{V}$. We then conserve those eigenvectors associated with the d nonzero eigenvalues,

$$\mathbf{W} = \mathbf{V}\mathbf{I}_{D\times d}, \tag{8}$$

which gives

$$\mathbf{C}_{\xi\xi} = \mathbf{I}_{d\times D}\boldsymbol{\Lambda}\mathbf{I}_{D\times d}. \tag{9}$$

We therefore conclude that the eigenvalues in $\boldsymbol{\Lambda}$ represent the variance of the latent variables (diagonal entries of $\mathbf{C}_{\xi\xi}$).

2.2. *Multidimensional Scaling, MDS*

PCA works with the covariance matrix of the experimental results, $\mathbf{Y}\mathbf{Y}^T$. However, multidimensional scaling, MDS, works with the Gram matrix containing scalar products, i.e., $\mathbf{S} = \mathbf{Y}^T\mathbf{Y}$ [8].

MDS preserves pairwise scalar products:

$$\mathbf{S} = \mathbf{Y}^T\mathbf{Y} = \boldsymbol{\Xi}^T\mathbf{W}^T\mathbf{W}\boldsymbol{\Xi} = \boldsymbol{\Xi}^T\boldsymbol{\Xi}. \tag{10}$$

Computing the eigenvalues of $\mathbf{S}$, we arrive at

$$\mathbf{S} = \mathbf{U}\boldsymbol{\Lambda}\mathbf{U}^T = \left(\mathbf{U}\boldsymbol{\Lambda}^{1/2}\right)\left(\boldsymbol{\Lambda}^{1/2}\mathbf{U}^T\right) = \left(\boldsymbol{\Lambda}^{1/2}\mathbf{U}^T\right)^T\left(\boldsymbol{\Lambda}^{1/2}\mathbf{U}^T\right), \tag{11}$$

which in turn gives

$$\boldsymbol{\Xi} = \mathbf{I}_{d\times M}\boldsymbol{\Lambda}^{1/2}\mathbf{U}^T. \tag{12}$$

2.3. *Kernel-Based Principal Component Analysis, k-PCA*

PCA is based on the fact that data not linearly separable in D dimensions, could be linearly separated if previously projected to a space in $Q > D$ dimensions. The true advantage comes, however, from the fact that it is not necessary to write down the analytical expression of that mapping.

The symmetric matrix $\boldsymbol{\Phi} = \mathbf{Z}^T\mathbf{Z}$, with $\mathbf{Z}$ containing the snapshots $\mathbf{z}_i \in \mathbb{R}^Q$, $i = 1,\cdots,\mathtt{M}$, associated with $\mathbf{y}_i \in \mathbb{R}^D$, has to be decomposed in eigenvalues and eigenvectors. The procedure for centering data $\mathbf{z}_i$ is done in an implicit way.

The eigenvector decomposition reads

$$\boldsymbol{\Phi} = \mathbf{U}\boldsymbol{\Lambda}\mathbf{U}^T, \tag{13}$$

giving rise to

$$\boldsymbol{\Xi} = \mathbf{I}_{d\times M}\boldsymbol{\Lambda}^{1/2}\mathbf{U}^T. \tag{14}$$

The difficulties of operating in a high-dimensional space of dimension, in general $Q \gg D$, and the mapping unavailability, are circumvented by introducing the kernel functional κ (also known as kernel trick) that allows computing scalar products in $\mathbb{R}^Q$ while operating in $\mathbb{R}^D$ by resorting to the Mercer theorem that establishes that, if $\kappa(\mathbf{u},\mathbf{v})$ (with $\mathbf{u} \in \mathbb{R}^D$ and $\mathbf{v} \in \mathbb{R}^D$) is continuous, symmetric and positive definite, then it defines an inner-product in the mapped space $\mathbb{R}^Q$. Many different kernels exist, some of them are reported in [8].

3. An illustrative case study

Imagine for a while a hypothetical mechanical system consisting of a prismatic beam whose three dimensions, height, width and length are noted respectively by h, b and L, all of them being measurable quantities. In what follows, we consider a particular output P that constitutes also a measurable quantity (e.g. buckling critical load, ...) assumed related to those parameters from an existing but actually hidden model, even if in what follows we will consider hypothetical, and most of the time, unphysical models.

Thus, we consider a set of data composed by $\mathtt{M}$ measures $\mathbf{y}_i = \{h_i,\ b_i,\ L_i, P_i\}$, $i = 1,\cdots,\mathtt{M}$, with h_i, b_i and L_i randomly chosen from a uniform probability distribution in their respective intervals of existence, $\mathscr{I}_h$, $\mathscr{I}_b$ and $\mathscr{I}_L$ respectively, defined from:

$$\begin{cases} \mathscr{I}_h = [h_{\min}, h_{\max}] \\ \mathscr{I}_b = [b_{\min}, b_{\max}] \\ \mathscr{I}_L = [L_{\min}, L_{\max}] \end{cases} \tag{15}$$

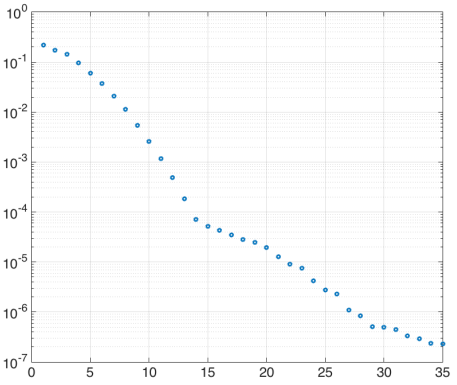

Figure 2. Eigenvalues $\lambda \in [\lambda_1 10^{-6}, \lambda_1]$.

Without any other pre-existing knowledge, one could expect the output depending on the three geometrical parameters, i.e., $P = P(h, b, L)$. In what follows we consider three different scenarios.

3.1. *Output depending on a single parameter*

In this section we assume a quite simple model that relates the output to a single parameter,

$$P = \alpha b, \quad \alpha \in \mathbb{R}^+, \tag{16}$$

with $\alpha = 1000$ in the numerical tests carried out. $\mathtt{M} = 1000$ measures are performed, with $\mathscr{I}_b \in [0.1, 0.2]$, $\mathscr{I}_b \in [0.15, 0.2]$ and $\mathscr{I}_L \in [1, 1.5]$.

The measures constitute a set of $\mathtt{M} = 1000$ points in $\mathbb{R}^4$, on which the k-PCA is applied, by using the Gaussian kernel

$$\kappa(\mathbf{y}_i, \mathbf{y}_j) = \exp^{-\frac{\|\mathbf{y}_i - \mathbf{y}_j\|^2}{2\beta^2}}, \tag{17}$$

with $\beta = 10$.

Fig. 2 depicts the highest eigenvalues among the $\mathtt{M}$ resulting from the k-PCA, the ones comprised between the highest one λ_1 and $10^{-6}\lambda_1$.

The slow manifold associated with $\boldsymbol{\xi}$ is represented by selecting the first three reduced coordinates (ξ_1, ξ_2, ξ_3), as shown in Fig. 3, where its one-dimensional intrinsic dimension is noticed. This result was expected from the considered model expressed in Eq. (16). The points on the slow-manifold were colored depending on the value of h, b, L or P, evidencing that b constitutes the latent variable and that the output P scales (visually) linearly with it.

One could be a bit surprised by the nonlinearity that the manifold exhibits despite of the model (16) linearity. This nonlinearity is an artifact of the used nonlinear kernel (17). Being the model linear, one could expect the ability of the PCA to address the problem at hand. For doing that, it suffices transforming the kernel into its linear counterpart giving rise to the PCA

$$\kappa(\mathbf{y}_i, \mathbf{y}_j) = \mathbf{y}_i \cdot \mathbf{y}_j. \tag{18}$$

In this case, as expected, a single nonzero eigenvalue results, and consequently the dimension of the reduced space reduces to one, i.e. $\boldsymbol{\xi} = \xi$. The associated manifold is depicted in Fig. 4.

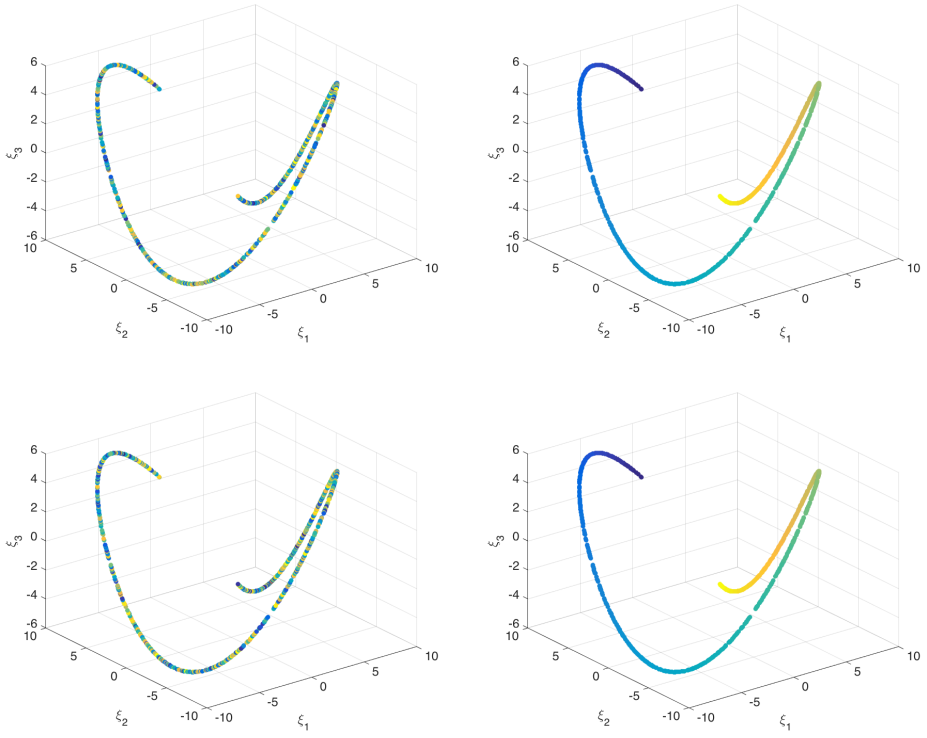

Figure 3. Slow-manifold in the 3D space defined by the first reduced coordinates (ξ_1, ξ_2, ξ_3). Each point is colored according to the value of the coordinate h (top-left), b (top-right), L (bottom-left) or P (bottom-right).

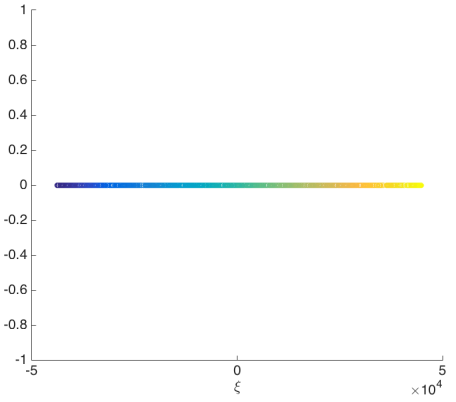

Figure 4. Slow-manifold ξ when considering the PCA linear dimensionality reduction. Again each point is colored according to the value of the variable b.

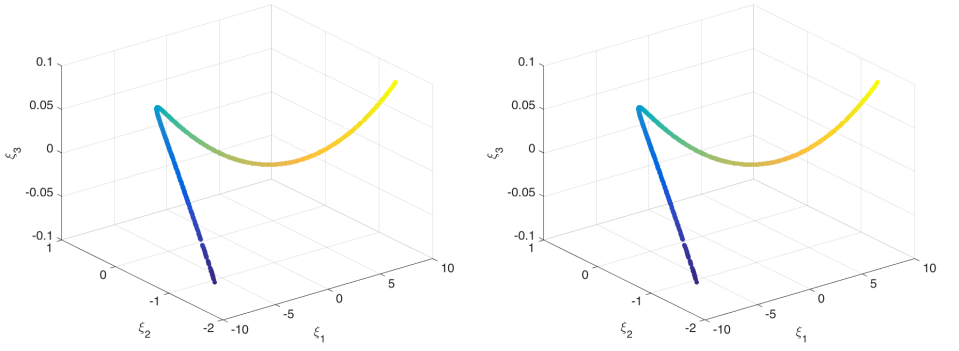

Figure 5. Slow-manifold in the 3D space defined by the three first reduced coordinates (ξ_1, ξ_2, ξ_3). Each point is colored according to the value of the coordinate h (left) or P (right).

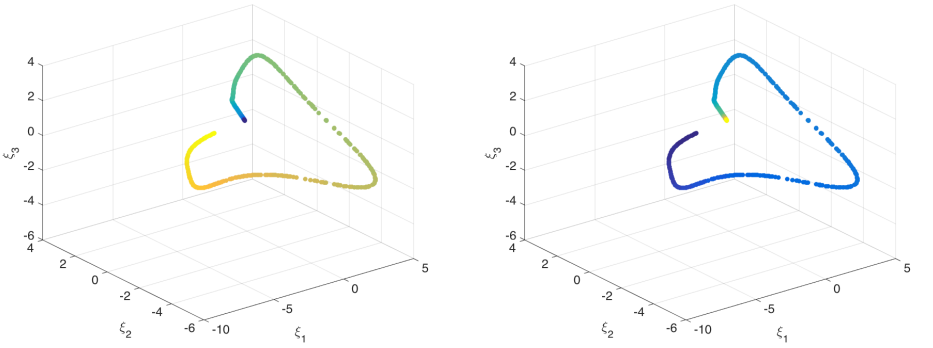

Figure 6. Slow-manifold in the 3D space defined by the three first reduced coordinates (ξ_1, ξ_2, ξ_3). Each point is colored according to the value of the coordinate L (left) or P (right).

Now, we consider a slightly different model, again depending on a single variable but in a nonlinear manner, according to

$$P = \alpha h^2, \tag{19}$$

with again $\alpha = 1000$. Fig. 5 depicts the one-dimensional slow-manifold where points are colored according to the value of variable h or P, where even if the direct relation can be noticed, its nonlinearity is much less evident to visualize.

Finally, we consider the model

$$P = \frac{\alpha}{L^2}, \tag{20}$$

with $\alpha = 1000$. Fig. 6 depicts the one-dimensional slow-manifold where points are colored according to the value of variable L or P, to emphasize the inverse relation between both them.

3.2. *Output depending on two parameters*

In this section we consider a model involving two of the three variables, in particular

$$P = \alpha \frac{h^3}{L^2}, \tag{21}$$

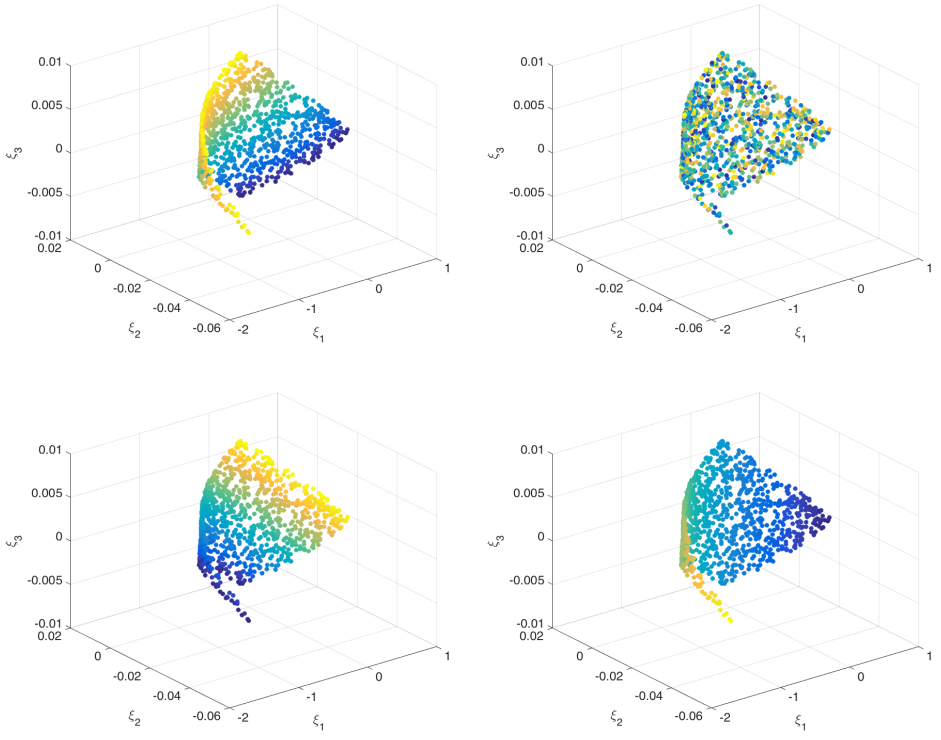

Figure 7. Slow-manifold in the 3D space defined by the three first reduced coordinates (ξ_1, ξ_2, ξ_3). Each point is colored according to the value of the coordinate h (top-left), b (top-right), L (bottom-left) or P (bottom-right).

with $\alpha = 1000$.

Fig. 7 depicts the two-dimensional slow-manifold where points are colored according to the value of variables h, b, L or P, where the direct and inverse effects of h and L with respect to P can be noticed, as well as the fact that parameter b seems, and in fact is, useless.

3.3. *Identifying hidden variables*

The previous case studies revealed the ability to extract the intrinsic dimensionality of the slow-manifold as well as the possibility to identify useless parameters. The present case addresses a very different situation in which the model involves the three variables, in the discussed case h, b and L, but only two of them were measured, namely h and L with the output P, b remaining inaccessible.

Thus, we have

$$P = \alpha \frac{bh^3}{L^2}, \tag{22}$$

with $\alpha = 1000$. Therefore, the $\mathtt{M} = 1000$ collected data $\mathbf{y}_i$, $i = 1, \cdots, \mathtt{M}$, read $\mathbf{y}_i = \{h_i, L_i, P_i\} \in \mathbb{R}^3$.

Fig. 8 depicts the reduced points (ξ_1, ξ_2, ξ_3) that as it can be noticed are distributed into a domain $\omega \subset \mathbb{R}^3$, but no dimensionality reduction is noticed. A direct consequence is that many values of the output P exist for the same values on the measured inputs h and L.

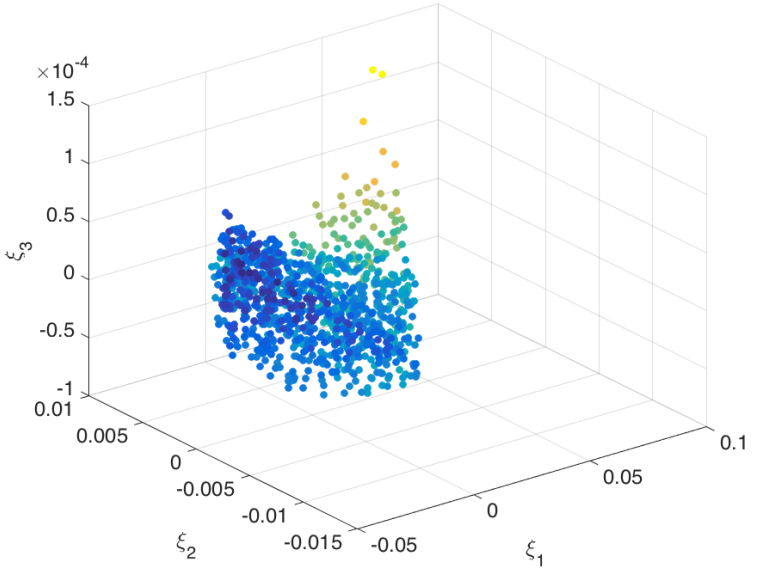

Figure 8. Reduced representation $\boldsymbol{\xi}_i \in \mathbb{R}^3$ of the data data $\mathbf{y}_i \in \mathbb{R}^3$, where the reduced points are colored according to the value of the output P.

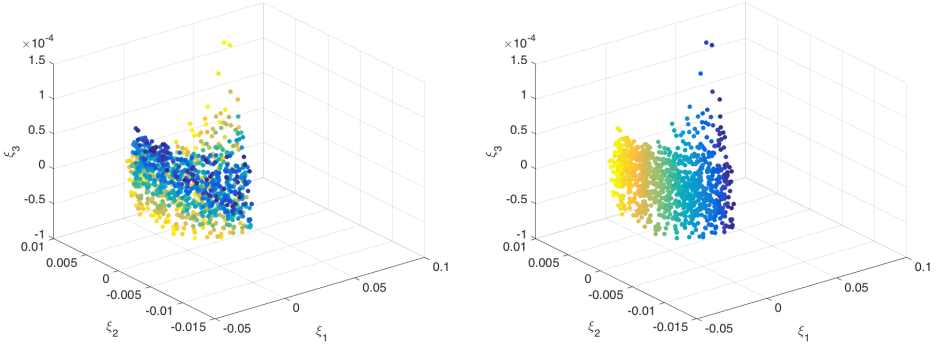

Figure 9. Reduced points colored according to the value of the coordinate h (left) or L (right).

Such a multi-valued output does not represent any conceptual difficulty. It indicates that even if both variables participate in the output, maybe there are others that were not considered or that maybe the ones considered are useless for explaining the output.

In order to conclude about the pertinence of these variables with respect to the considered output, we consider coloring the reduced data depending on the h and L values (refer to Fig. 9), and compare them with the one where color scales with the output P reported in Fig. 8.

Thus, one could conclude that both variables h and L are relevant for explaining the output P. If we assume—it is our choice and freedom as scientists—that the output P should be univocally explained from a small number of variables, clearly only two (here h and L) are not enough. One

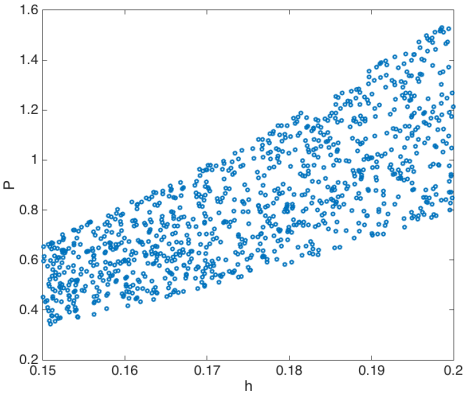

Figure 10. Data-set $\mathbf{y}_i = \{h_i, P_i\}$, $i = 1, \ldots, \mathtt{M}$.

extra-dimension suffices for recovering a single-valued output, that is, considering the reduced points in four dimensions $\mathbb{R}^4$.

As visualizing things in four dimensions is quite a difficult task, for the sake of clarity in the exposition, we propose in what follows, addressing a simpler model implying lower dimensional spaces.

We consider the simpler model

$$P = \alpha b h^3, \tag{23}$$

with $\alpha = 1000$. However, the $\mathtt{M} = 1000$ collected data $\mathbf{y}_i$, $i = 1, \cdots, \mathtt{M}$, only concern h and P, i.e. $\mathbf{y}_i = \{h_i, P_i\} \in \mathbb{R}^2$.

Fig. 10 depicts the data set $\mathbf{y}_i = \{h_i, P_i\}$, where it can be noticed that many values of the output P are found for the same value of variable h.

For univocally expressing the output P we consider again the k-PCA and compute the reduced data-set in a 3D space by considering the three first coordinates (ξ_1, ξ_2, ξ_3), while coloring these points with respect to h, to prove that h represents an explanatory variable, or with respect to P (refer to Fig. 11). Figure 12 depicts the same manifold but now colored by using the hidden variable b, that proves that it contributes to explain the output P and constitutes the hidden variable.

Obviously there is not a unique choice. The same behavior is obtained by coloring the reduced data-set with respect to any function $b^p h^q$, with $p, q \in \mathbb{R}$. Thus, any measurable variable ensuring such an uniform color grading could be used as latent variable for constructing the model. There is an infinite number of possibilities, but with certain constraints, in the present case it must involve b.

To finish this section, we are addressing a similar but more complex situation. We consider now the richer model

$$P = \alpha \frac{b h^3}{L^2}, \tag{24}$$

with $\alpha = 1000$. The $\mathtt{M} = 1000$ collected data $\mathbf{y}_i$, $i = 1, \ldots, \mathtt{M}$, only concern the input variable h and the output P, i.e. $\mathbf{y}_i = \{h_i, P_i\} \in \mathbb{R}^2$, with two variables involved in the model (24) remaining hidden, b and L.

Fig. 13 depicts the data-set $\mathbf{y}_i = \{h_i, P_i\}$, where again it can be noticed that many values of the output P are found for the same value of the variable h.

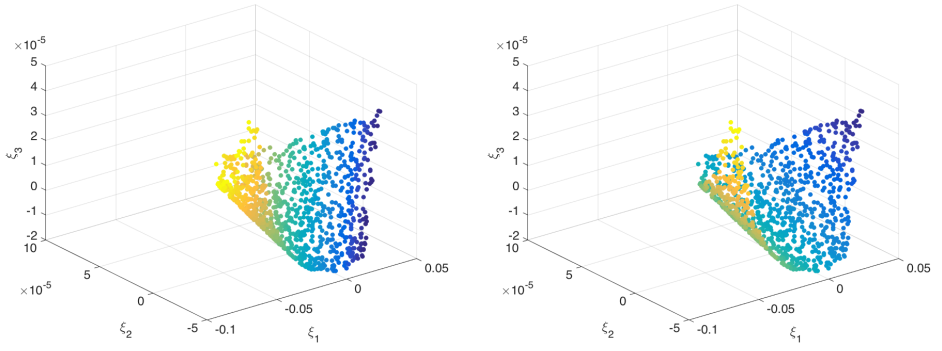

Figure 11. Reduced points colored according to the value of the coordinate h (left) or P (right).

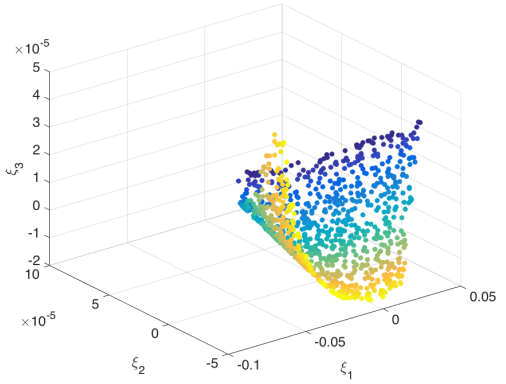

Figure 12. Reduced points colored according to the value of the output b.

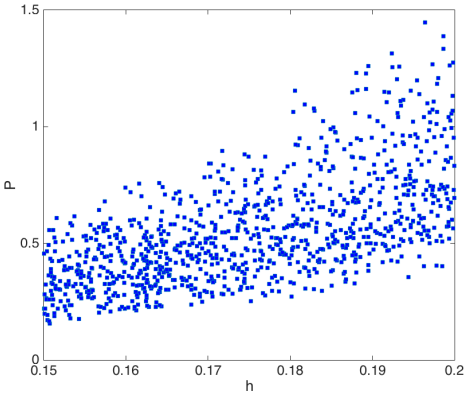

Figure 13. Data-set $\mathbf{y}_i = \{h_i, P_i\}$.

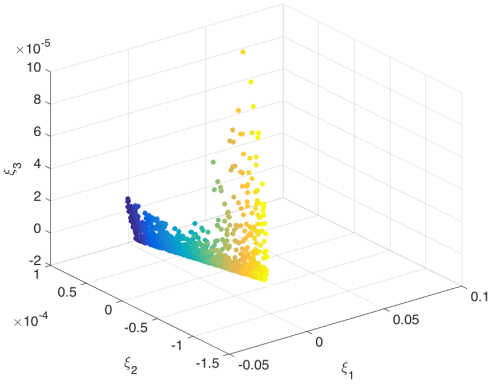

Figure 14. Reduced points colored according to the value of the coordinate h.

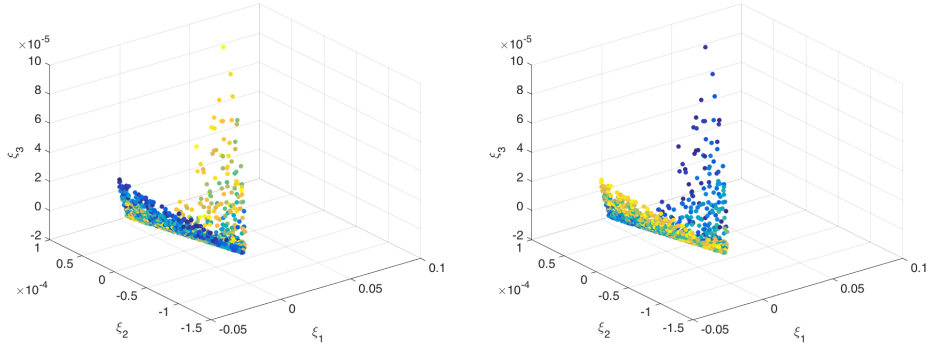

Figure 15. Reduced points colored according to the value of the variable b (left) or L (right).

For univocally expressing the output P we consider again the k-PCA and compute the reduced data-set in a 3D space by considering again the three first coordinates (ξ_1, ξ_2, ξ_3), while coloring these points with respect to h to prove that h represents an explanatory variable of the output P, as Fig. 14 proves. Figure 15 clearly reveals, by coloring the reduced points with respect to the two variables b and L, taken solely, that they do not represent the unique hidden variable able to explain, with h, the output P. The hidden latent variable according to the model (24) should combine b and h, and Fig. 16 proves that the combined parameter b/L^2 perfectly works, when compared with the manifold colored with respect to the output P.

It is important to note that the latent variable must involve the term b/L^2 to any power, and eventually multiplied by any power of h.

4. Simple mechanical behaviors

In this section we consider some simple one-dimensional mechanical behaviors, as the one depicted in Fig. 17. Figure 18 shows a set of $\mathtt{M} = 1500$ strain-stress pairs $\mathbf{y}_i = \{\varepsilon_i, \sigma_i\}$, $i = 1, \ldots, \mathtt{M}$, related to an hypothetical one-dimensional elastic-plastic behavior with linear hardening. The depicted points represent the final mechanical state (strain-stress) of $\mathtt{M}$ loading-unloading random

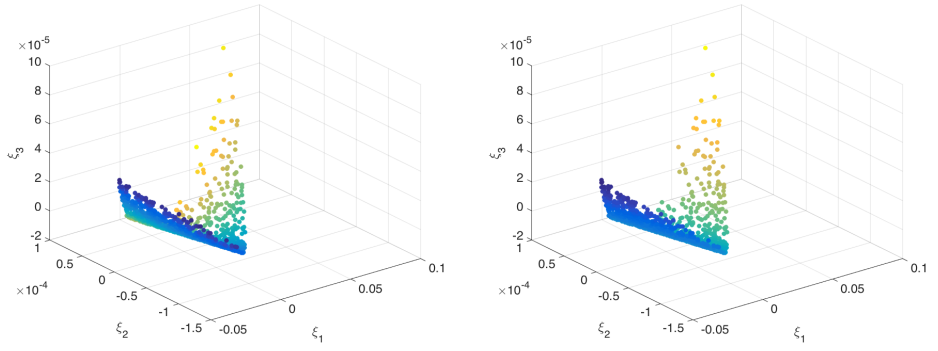

Figure 16. Reduced points colored according to the value of the variable b/L^2 (left) or P (right).

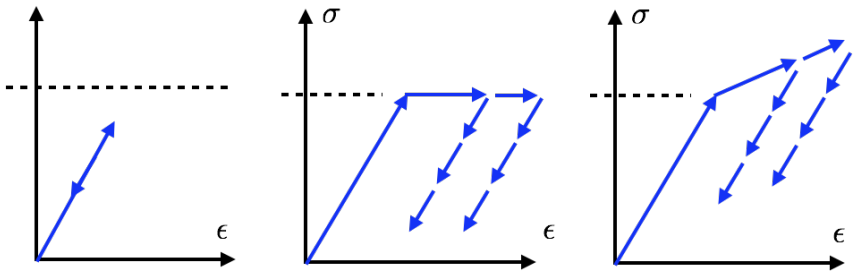

Figure 17. Elastic behavior (left), elastic perfectly plastic behavior (center) and elasto-plasticity with linear hardening (right).

trajectories. It can be noticed that with the only information of possible mechanical states, given a strain there are many possible values of admissible stresses and vice-versa.

There is nothing physically inconsistent in the fact of having multivalued fields, but if one is looking for a single valued stress, then an extra latent variable must be introduced.

If, as in the previous section, we apply the k-PCA on the data-set $\mathbf{y}_i$, $i = 1,\ldots,\mathtt{M}$, as expected the 2D manifold appears embedded in the $\mathbb{R}^3$ space, as depicted in Fig. 19, a fact that indicates that three mechanical variables, the stress and strain completed with a latent extra-variable p, are mutually related, e.g. $\sigma = \sigma(\varepsilon, p)$, giving rise to a 2D manifold embedded in $\mathbb{R}^3$.

As previously discussed, many latent variables could be certainly considered for obtaining for example a single-valued stress. Historically, the plastic strain ε_p, sketched in Fig. 20, was widely considered as latent variable. By coloring the reduced points $\boldsymbol{\xi}_i$ depicted in Fig. 19 according to the plastic strain, there results the colored manifold shown in Fig. 21, that validates the choice of the plastic strain as latent variable.

5. Towards alternative representations of the mechanical state

An alternative representation of the mechanical state, avoiding the choice of non-evident latent variables, consists of assuming that the stress at time t depends on all the strain history, that is on $\varepsilon(\tau)$, $\tau \leq t$.

When memory effects are neglected, the mechanical state could be described at time t from the strain and stress increments and the stress-strain present state, that is, $\forall t_i = i\Delta t$, $\mathbf{y}_i =$

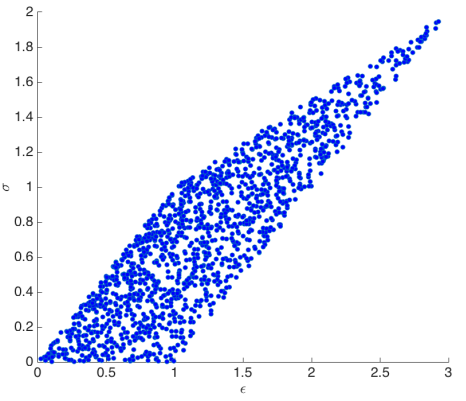

Figure 18. Strain-stress mechanical states related to an elastic-plastic behavior with linear hardening.

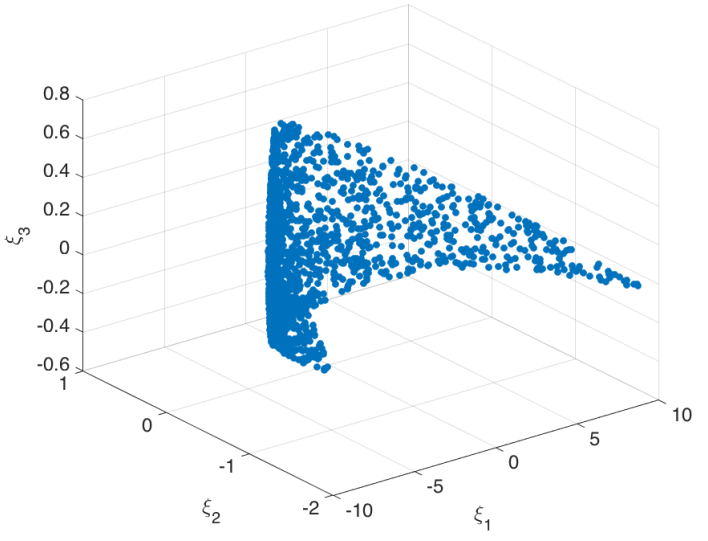

Figure 19. Elastic-plastic manifold embedded into the 3D space.

$\{\varepsilon_i, \sigma_i, \Delta\sigma_i/\Delta\varepsilon_i\}$ with $\Delta\varepsilon_i$ of given magnitude and two possible signs (positive in loading and negative in unloading).

Different scenarios can be analyzed:

- Linear elastic regime without plastic strain. In this case as expected, the slow manifold constituted by the reduced stales $\boldsymbol{\xi}_i$ related to the mechanical states $\mathbf{y}_i$, depicted in Fig. 22 in the 3D space (ξ_1, ξ_2, ξ_3) becomes one-dimensional.
- Nonlinear elastic behavior (with the tangent modulus $E_T = E\varepsilon^2$) without plastic strain. In this case the results are similar to the ones just discussed, but now in Fig. 23 the nonlinear behavior can be noticed.
- Linear elastic regime with nonzero plastic strain (perfect plasticity—no hardening—). In

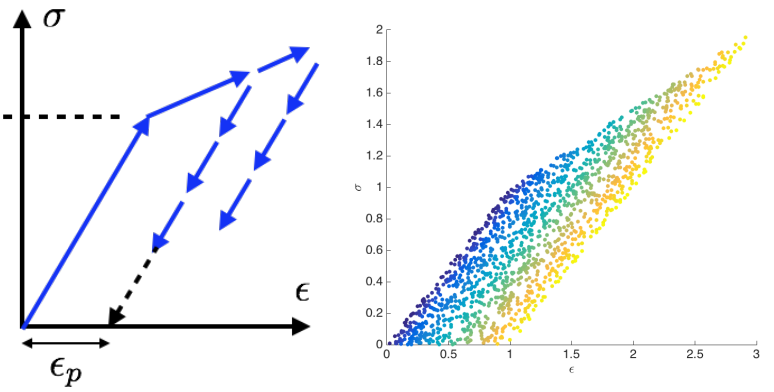

Figure 20. Plastic strain definition (left) and mechanical states $\mathbf{y}_i$ colored according to the plastic strain (right).

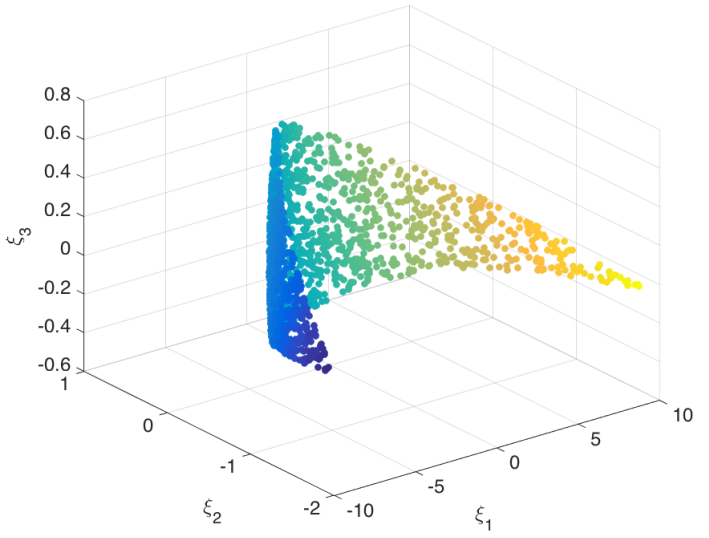

Figure 21. Manifold colored according to the plastic strain.

the present case, with the mechanical state within the elastic domain, we recover from $\mathbf{y}_i$ a reduced slow-manifold of dimension two, as expected, depicted in Fig. 24.

- Linear elastic regime with nonzero plastic strain (perfect plasticity—no hardening—) with activated damage. In the present case with respect to the previous discussed scenario, we consider that the material degrades with the magnitude of the plastic strain and the tangent modulus reduces accordingly. As Fig. 25 depicts, things are quite similar to the previous scenario, but now, when coloring with respect to the tangent modulus, the expected uniform degraded map is noticed.
- The present case study considers, in addition of the points inside the elastic domain, another set of mechanical states on the elastic domain boundary with a different instantaneous tangent modulus when loading and unloading. As Fig. 26 reveals, the mechan-

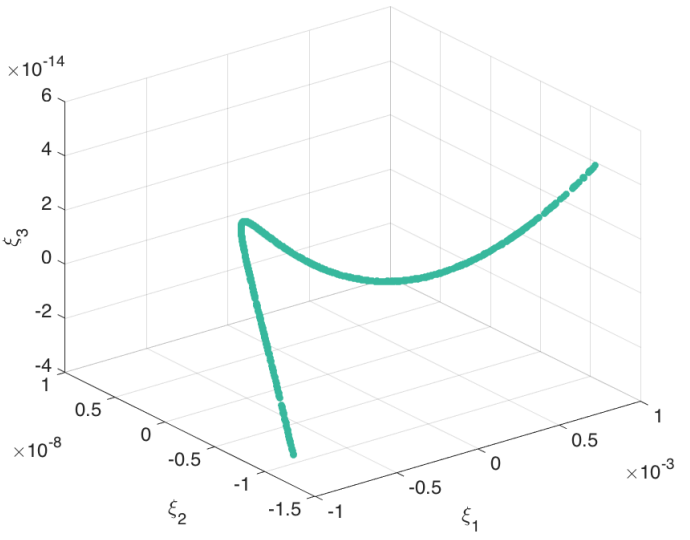

Figure 22. Slow-manifold related to a linear elastic behavior and colored according to the tangent modulus, i.e. $\Delta\sigma_i/\Delta\varepsilon_i$.

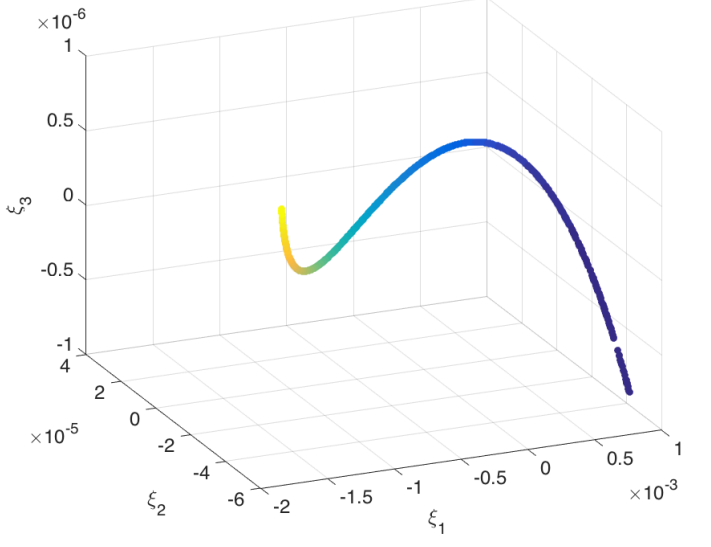

Figure 23. Slow-manifold related to a nonlinear elastic behavior and colored according to the tangent modulus, i.e. $\Delta\sigma_i/\Delta\varepsilon_i$.

ical manifold is now richer with points on the elastic domain boundary separated from the elastic manifold. In the solution depicted in Fig. 26, damage was not activated. In the presence of damage, elastic tangent modulus reduction scaling with the plastic strain, the slow-manifold colored according to the tangent modulus is shown in Fig. 27.

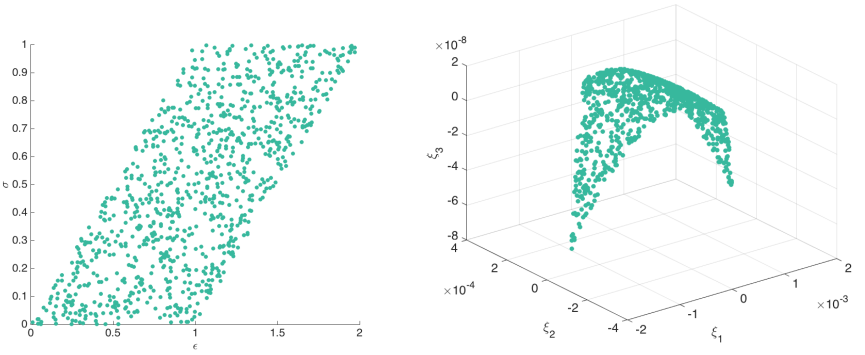

Figure 24. Strain-stress points associated to states within the elastic domain with nonzero plastic strains (left) and associated slow-manifold colored according to the tangent modulus (right).

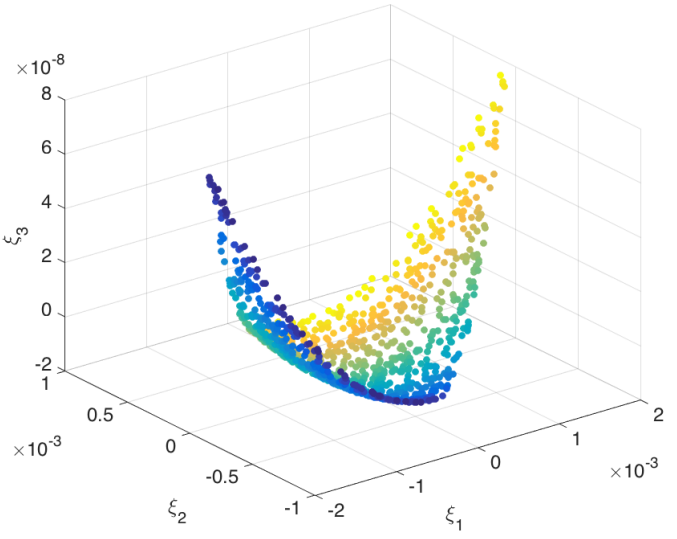

Figure 25. Slow-manifold related to a damageable elastic-plastic behavior operating within the elastic domain colored according to the tangent modulus.

- The last scenario adds an extra-richness to the constitutive behavior. At the mechanical states within the elastic domain, the elastic tangent modulus is affected by a latent variable that consist of the product of the plastic strain with another extra-variable. The last, that could represent a strain-rate sensitivity, is here assumed taking arbitrary values, due to the fact that we are more interested in the methodological aspects than in physical considerations. The considered mechanical states are depicted in Fig. 28. When applying the k-PCA on the set of mechanical states $\mathbf{y}_i = \{\varepsilon_i, \sigma_i, \Delta\sigma_i/\Delta\varepsilon_i\}$ the resulting manifold remains 3D. As expected, no dimensionality reduction is accomplished, as Fig. 29 reveals, where many values of the elastic tangent modulus can be found for the same values of the stress and strain. To investigate the nature of that behavior, we depict in Fig. 30 the elastic

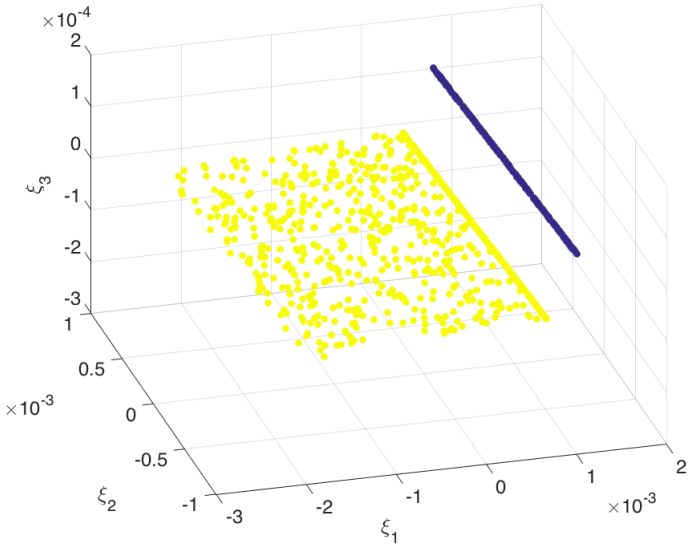

Figure 26. Slow-manifold related to an elastic-plastic behavior operating within the elastic domain and on the elastic domain boundary colored according to the tangent modulus.

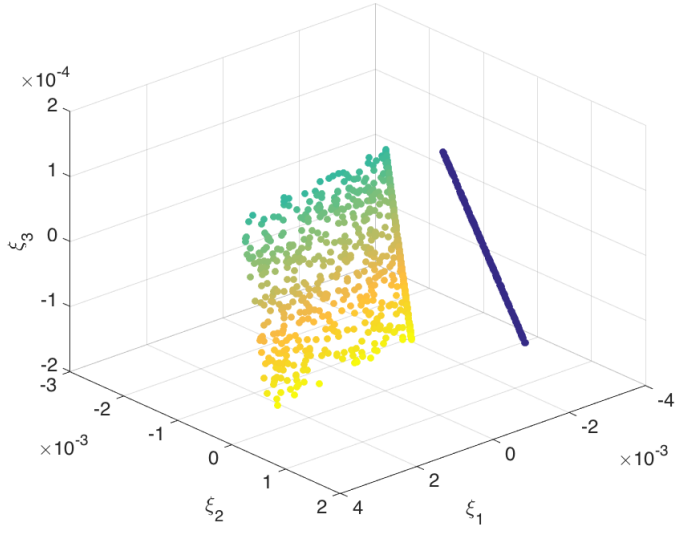

Figure 27. Slow-manifold related to an elastic-plastic behavior operating within the elastic domain and on the elastic domain boundary, colored according to the tangent modulus, when damage is activated.

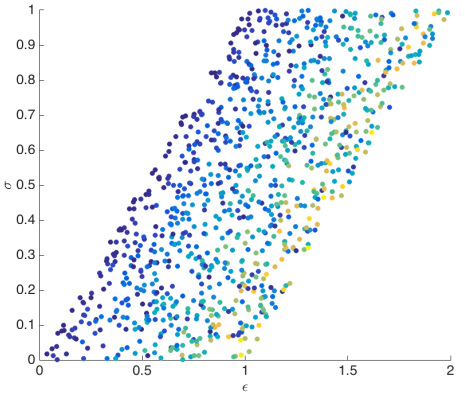

Figure 28. Mechanical states within the elastic domain, colored according to the tangent modulus, the last depending on the product of two latent variables, the plastic strain and another arbitrarily chosen.

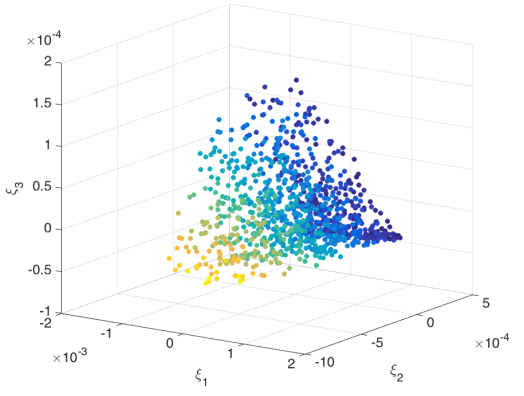

Figure 29. Slow-manifold related to an elastic-plastic behavior operating within the elastic domain, colored according to the tangent modulus, with the last scaling with the product of the plastic strain and an extra-latent variable.

tangent modulus versus the plastic strain, where as expected it can be noticed that the former does not depend exclusively on the last. By applying the k-PCA to the data shown in Fig. 30, non-separable in two dimensions, one expects separating it by embedding in a three-dimensional space, as previously discussed, and as Fig. 31 proves. Finally, Fig. 32 presents the slow-manifold of Fig. 31 but now colored with respect to the plastic-train and the extra-latent variable.

6. Conclusion

The present work introduced, tested and discussed issues related to the manifold dimensionality, with two major purposes: (i) first, when too many measurable variables are employed, manifold learning is able to discard the useless ones; (ii) second and more importantly, the same technique,

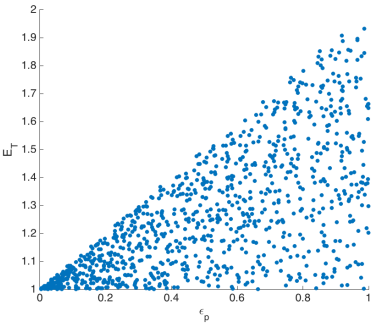

Figure 30. Elastic tangent modulus versus the plastic strain.

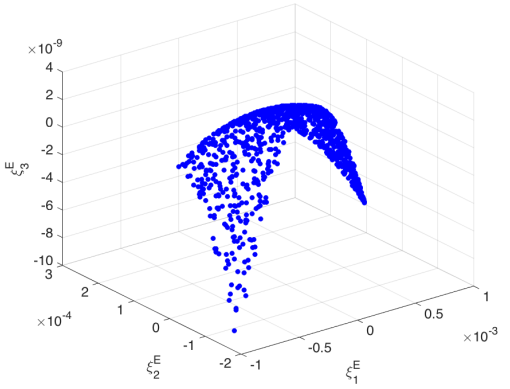

Figure 31. Slow-manifold related to the data consisting of the elastic tangent modulus and plastic strain.

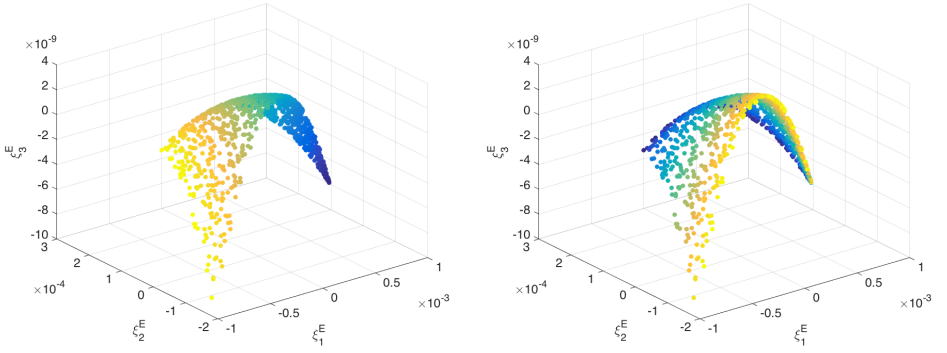

Figure 32. Slow-manifold of the elastic tangent modulus colored according to the plastic-strain (left) and the extra-latent variable (right).

can be employed for discovering the necessity of employing and then measuring an extra-latent variable able to recover and ensure single-valued outputs.

Indeed, the physical interpretation of that discovered latent variable could imply the introduction of other measurable ones. This topic should be deeply analyzed.

The main interest of discovering those manifolds is that for a new accessible mechanical state, the output can be inferred by a simple interpolation from its neighbors on the manifold. The main aim of the present work was the contruction and analysis of those manifolds. Future works, currently in progress, will focus on their use for performing data-driven simulations.

Conflicts of interest

The authors declare no competing financial interest.

Dedication

The manuscript was written through contributions of all authors. All authors have given approval to the final version of the manuscript.

Acknowledgments

The first, third and fourth authors are supported by their respective ESI Group research chairs, whose support are gratefully acknowledged.

References

[1] A. Badias, S. Curtit, D. Gonzalez, I. Alfaro, F. Chinesta, E. Cueto. An Augmented Reality platform for interactive aerodynamic design and analysis. Internat. J. Num. Meth. Engrg. In press.

[2] M.A. Bessa, R. Bostanabad, Z. Liu, A. Hu, Daniel W. Apley, C. Brinson, W. Chen, W.K. Liu. A framework for data-driven analysis of materials under uncertainty: Countering the curse of dimensionality. Computer Methods in Applied Mechanics and Engineering, 320, 633-667, 2017.

[3] D. Gonzalez, F. Chinesta, E. Cueto. Thermodynamically consistent data-driven computational mechanics. 31, 239-253, 2019.

[4] R. Ibanez, E. Abisset-Chavanne, J.V. Aguado, D. Gonzalez, E. Cueto, F. Chinesta. A manifold learning approach to data-driven computational elasticity and inelasticity. Archives of Computational Methods in Engineering, 25(1), 47-57, 2018.

[5] N. Kambhatla, T.K. Leen. Dimension reduction by local principal component analysis. Neural Computation, 9(7),1493-1516, 1997.

[6] T. Kirchdoerfer, M. Ortiz. Data-driven computational mechanics. Computer Methods in Applied Mechanics and Engineering, 304, 81-101, 2016.

[7] M. Latorre, F.J. Montans. What-you-prescribe-is-what-you-get orthotropic hyperelasticity. Computational Mechanics, 53(6), 1279-1298, 2014.

[8] J.A. Lee, M. Verleysen. Nonlinear dimensionality reduction. Springer, New York, 2007.

[9] Z. Liu, M. Fleming, W.K. Liu. Microstructural material database for self-consistent clustering analysis of elastoplastic strain softening materials. Computer Methods in Applied Mechanics and Engineering, 330, 547-577, 2018.

[10] L. Maaten, G. Hinton. Visualizing data using t-SNE. J Mach Learn Res., 9, 2579-2605, 2008.

[11] S.T. Roweis, L.K. Saul. Nonlinear dimensionality reduction by locally linear embedding. Science, 290(5500), 2323-2326, 2000.

[12] Z. Zhang, H. Zha. Principal manifolds and nonlinear dimensionality reduction via tangent space alignment. SIAM J. Sci. Comput., 26(1), 313-338, 2005.